PNAS RESEARCH ARTICLE | EARTH, ATMOSPHERIC, AND PLANETARY SCIENCES

Microscopic defect dynamics during a brittle-to-ductile transition

Hoagy O'Ghaffari[a,1], Matěj Peč[a,1], Tushar Mittal[a,2], Ulrich Mok[a], Hilary Chang[a], and Brian Evans[a]

Edited by David Kohlstedt, University of Minnesota, Minneapolis, MN; received April 7, 2023; accepted August 18, 2023

Deformation of all materials necessitates the collective propagation of various microscopic defects. On Earth, fracturing gives way to crystal-plastic deformation with increasing depth resulting in a "brittle-to-ductile" transition (BDT) region that is key for estimating the integrated strength of tectonic plates, constraining the earthquake cycle, and utilizing deep geothermal resources. Here, we show that the crossing of a BDT in marble during deformation experiments in the laboratory is accompanied by systematic increase in the frequency of acoustic emissions suggesting a profound change in the mean size and propagation velocity of the active defects. We further identify dominant classes of emitted waveforms using unsupervised learning methods and show that their relative activity systematically changes as the rocks cross the brittle–ductile transition. As pressure increases, long-period signals are suppressed and short-period signals become dominant. At higher pressures, signals frequently come in avalanche-like patterns. We propose that these classes of waveforms correlate with individual dominant defect types. Complex mixed-mode events indicate that interactions between the defects are common over the whole pressure range, in agreement with postmortem microstructural observations. Our measurements provide unique, real-time data of microscale dynamics over a broad range of pressures (10 to 200 MPa) and can inform micromechanical models for semi-brittle deformation.

rock deformation | brittle–ductile transitions | defect dynamics | ultrasound probes

Significance

Rocks close to the surface fracture, whereas rocks at depths flow implying the existence of a "brittle-to-ductile" transition (BDT) region. This region is key in several Earth science applications and yet remains poorly understood. Whether rocks fracture or flow is fundamentally determined by the activity of various microscale defects. Given that these defects are microscopic and typically need high pressures and temperatures to be activated, it remains a challenge to observe the defect dynamics in situ. Here, we present observations of such defect dynamics in rocks undergoing a BDT. Using ultrasound probes, we document that the nature, size, and propagation velocity of defects profoundly changes as the rocks cross their BDT, providing constraints for micromechanical models of semi-brittle deformation.

The strength of the lithosphere is limited by pressure-dependent, "brittle" deformation of the upper crust and temperature- and strain-rate-dependent "ductile" deformation in the lower crust and upper mantle (1, 2). From a simplified mechanistic point of view, intersection of these two strength envelopes can be used to estimate the depth of a region known as the brittle-to-ductile transition (BDT) where rocks deform by semi-brittle flow (3, 4). This region is associated with changes in 1) dominant deformation mechanisms, 2) strain localization, and 3) fault stability (5–7); however, the transitions in all three attributes are influenced by many parameters, including lithology, grain size, porosity, the presence and migration of pore fluids, the loading conditions, metamorphic reactions, and the geometric complexities of geologic formations and faults. Thus, the transitions in deformation mechanisms, failure mode, and stability do not typically occur simultaneously, resulting in complex behavior that is poorly understood. Developing appropriate rheological laws for the brittle to ductile transition is critical for understanding solid-earth processes ranging from plate boundary deformation, slow slip (8), continental and oceanic rifting (9), and vertical magmatic transport and eruptibility (10).

The fundamental agents of deformation that control rock strength are microscale defects such as point defects, dislocations, twins, grain boundaries, and cracks (11, 12). Their collective motion under stress leads to the emergence of larger-scale features that ultimately determine whether rocks fracture or flow during tectonic processes (1, 2). Laboratory studies under well-controlled conditions provide the best opportunity for constraining the activity and interactions of defect populations that lead to the emergence of brittle or ductile deformation on the macroscale (3, 12–15). In addition, a laboratory-based constitutive law is the first step to a more sophisticated understanding of natural processes (16). One important technique is to examine the microstructural fingerprints of defects frozen into the structure after deformation has ceased (17). But such postmortem structures give only a time-integrated perspective of microscale dynamics and are not sufficient to constrain the defect dynamics occurring at a given time as stress–strain conditions evolve especially in conditions with complex multidefect interactions.

Deformation of calcite marbles exhibits a BDT in laboratory experiments at room temperature with increasing pressure (7, 18–20) because calcite requires only low resolved shear stresses to nucleate crystal-plastic deformation (21, 22). Postmortem microstructural studies document the co-occurrence of twinning, fracturing, and dislocation glide in the semi-brittle flow regime (3, 18). However, real-time, in situ signatures of the microscale defects involved in a BDT of a rock sample have been, until now, experimentally

Author affiliations: [a]Department of Earth, Atmospheric and Planetary Sciences, Massachusetts Institute of Technology, Cambridge, MA 02139

Author contributions: H.O. and M.P. designed research; H.O., M.P., T.M., U.M., and H.C. performed research; H.O., T.M., and H.C. contributed new reagents/analytic tools; H.O., M.P., T.M., U.M., H.C., and B.E. analyzed data; and H.O., M.P., and T.M. wrote the paper.

The authors declare no competing interest.

This article is a PNAS Direct Submission.

[1]To whom correspondence may be addressed. Email: hoghaff@mit.edu or mpec@mit.edu.

[2]Present address: Department of Geosciences, Pennsylvania State University, University Park, PA 16802.

This article contains supporting information online at https://www.pnas.org/lookup/suppl/doi:10.1073/pnas.2305667120/-/DCSupplemental.

Published October 9, 2023.

inaccessible. We show here that spontaneously emitted ultrasonic waves, i.e., acoustic emissions (AEs), exhibit profound changes that can be related to the dynamics of nucleation and propagation of defects in marbles as they cross a BDT. Observing the collective behavior of microscale defects during the experiments provides a pathway for understanding the deformation process and formulating accurate rheological models relevant for semi-brittle rheology. The length- and time- scales involved in a deformation process are critical input parameters for models of both brittle (23, 24) as well as ductile (25) creep and failure (See *SI Appendix, Supplementary Text* for more discussion).

Results

For this study, we deformed cylindrical samples of dry Carrara marble at room temperature in a gas medium deformation apparatus under conventional triaxial loading. We applied confining pressures ranging from 10 MPa to 200 MPa which is sufficient to cross the BDT (typically 60 to 80 MPa at room temperature). In all our experiments, we used two custom-made, miniature piezosensors on top and bottom of the sample, covering accumulatively a broad range of frequencies from 70 kHz to 65 MHz. We used these sensors in both "passive", listening mode as well as "active", pulse transmission mode (*Materials and Methods*). The number of AEs, observation of the waveforms, and the evolution of longitudinal wave velocity (v_p) give us insight about microstructural changes occurring during deformation. In this study and in previous work (19, 26), v_p decays rapidly during deformation, suggesting that the elastic moduli of the rocks decrease as damage is accumulated; this decay is much less pronounced at higher pressures (for example, see Fig. 1).

To study the complex interaction of microscale defects during rock deformation, we analyze the AE datasets in a hierarchical manner. We start with local clustering of waveforms into Classes, investigating each individual experiment separately. This analysis provides insight about how dominant microstructural defect processes evolve with changing stress–strain conditions at one confining pressure. Next, we perform a global clustering of the data into Clusters using AEs from all experiments together. This type of analysis elucidates the changes in defect dynamics across the brittle–ductile transition as the rocks are deformed at progressively higher and higher confining pressures. Finally, we aggregate the global clusters into a few dominant Types, based on waveform characteristics, as a potential first-order proxy for different categories of microstructural defects (e.g., cracks, twins, dislocations). More details of the hierarchical analyses are given in the *Materials and Methods* section.

As examples of the local clustering results, we first look closely at the extremes of confining pressure: 10 and 200 MPa. At 10 MPa confining pressure the sample reaches a peak strength of ~80 MPa and then weakens to ~30 MPa as a macroscopic fault develops (Fig. 1 and *SI Appendix*, Fig. S1). The waveforms emitted during each experiment are quantified using Dynamic Time Warping (DTW) and hierarchical clustering algorithms (aligned directly with our conceptual analysis methodology) aimed at revealing distinguishing characteristics (*Materials and Methods*). Two main representative AE classes are observed at 10 MPa confining pressure: long-duration events reminiscent of cracking in traditional rock mechanics experiments (27, 28) (Fig. 1*C*, class A) and short, impulsive events (Fig. 1*C*, classes B and C). Note that examples of both classes occur throughout the experiment. At 200 MPa confining pressure the sample is much stronger and reaches a peak strength of ~330 MPa followed by minor weakening. The sample barreled, but no macroscopic fault developed (*SI Appendix*, Fig. S1). All AEs have approximately an order of magnitude shorter duration than at low pressures (Fig. 1) and exhibit a stronger clustering with strain (i.e., E class events with relatively lower frequency predominantly occur at low and high strains while D and F class events, with the highest frequencies, occur at intermediate strains). AEs also frequently include multiple subevents within one triggered time window, particularly at high pressures (Fig. 1*D*, class F). These subevents are likely a direct signature of defect interactions (e.g., clusters of dislocations being triggered in an avalanche-type manner).

A correlation between AE types and different deformation mechanisms is supported by our microstructural analysis. The

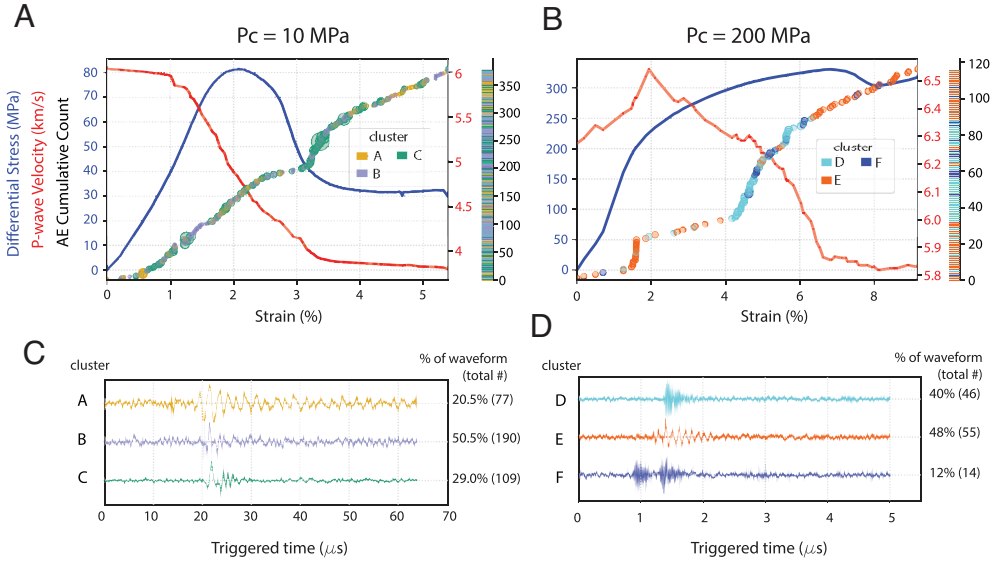

Fig. 1. Mechanical and acoustic data. (*A* and *B*) Cumulative AE hits coplotted with stress–strain curves and v_p evolution for samples deformed under confining pressures of 10 and 200 MPa. Size of the circles indicates the maximum local amplitude of the AEs. The color of individual circles as well as the color bar by AE count visualizes the occurrence of AE classes with respect to the mechanical data. Only classes with >1% of AEs are shown. (*C* and *D*) Clustering of data reveals characteristic waveforms. Note the decrease in duration and increase in frequency of the AEs as pressure increases (triggered time window *x* axis shrinks from 70 μs to 5 μs).

density of crystal-plastic defects, as indicated by twins and slip-lines (i.e., lattice planes along which many dislocations propagated), increases significantly at higher pressures (*SI Appendix*, Fig. S2 and *Materials and Methods*). For example, at low pressures, the regions of intense damage, including crystal-plastic defects and crack damage, are localized around the macroscopic fault. Whereas at elevated pressures—where no macroscopic fault developed—these damaged areas are more homogenously distributed throughout the section. Thus, the total defect density increases significantly with increasing confining pressure (*SI Appendix*, Fig. S2); notice that increases in confining pressure also correspond to increased differential stresses (Fig. 1) and, hence, increased input of strain energy into the sample.

We further quantify the patterns of ~1,250 recorded AEs from all experiments and perform global clustering which necessitates further waveform conditioning to account for large frequency shifts observed during the experiments, see *Materials and Methods*. In particular, we are interested in analyzing changes in waveform shapes, independent of the AE frequency and amplitude shifts across the different experiments. In Fig. 2, we plot typical waveforms for main types of events together with the distance matrix for all events.

Type I events are contained in cluster 1 which includes events that occur dominantly at low differential stresses, low strain, and low v_p (note that initial v_p increases with increasing confining pressure; see *SI Appendix, Supplementary Text*). Some waveforms in this cluster were observed over the whole studied confining pressure range (Fig. 2*B* and *SI Appendix*, Fig. S3). These events are typically in the range of 400 kHz to 7 MHz and have durations that often exceed 5 μs.

Type II events are formed by clusters 2, 3, and 4 that have shorter durations, an abrupt impulsive onset, and higher frequencies compared to type I events (Fig. 2*A*). Because the waveforms are, in a smoothed form, characterized by the same types of shape

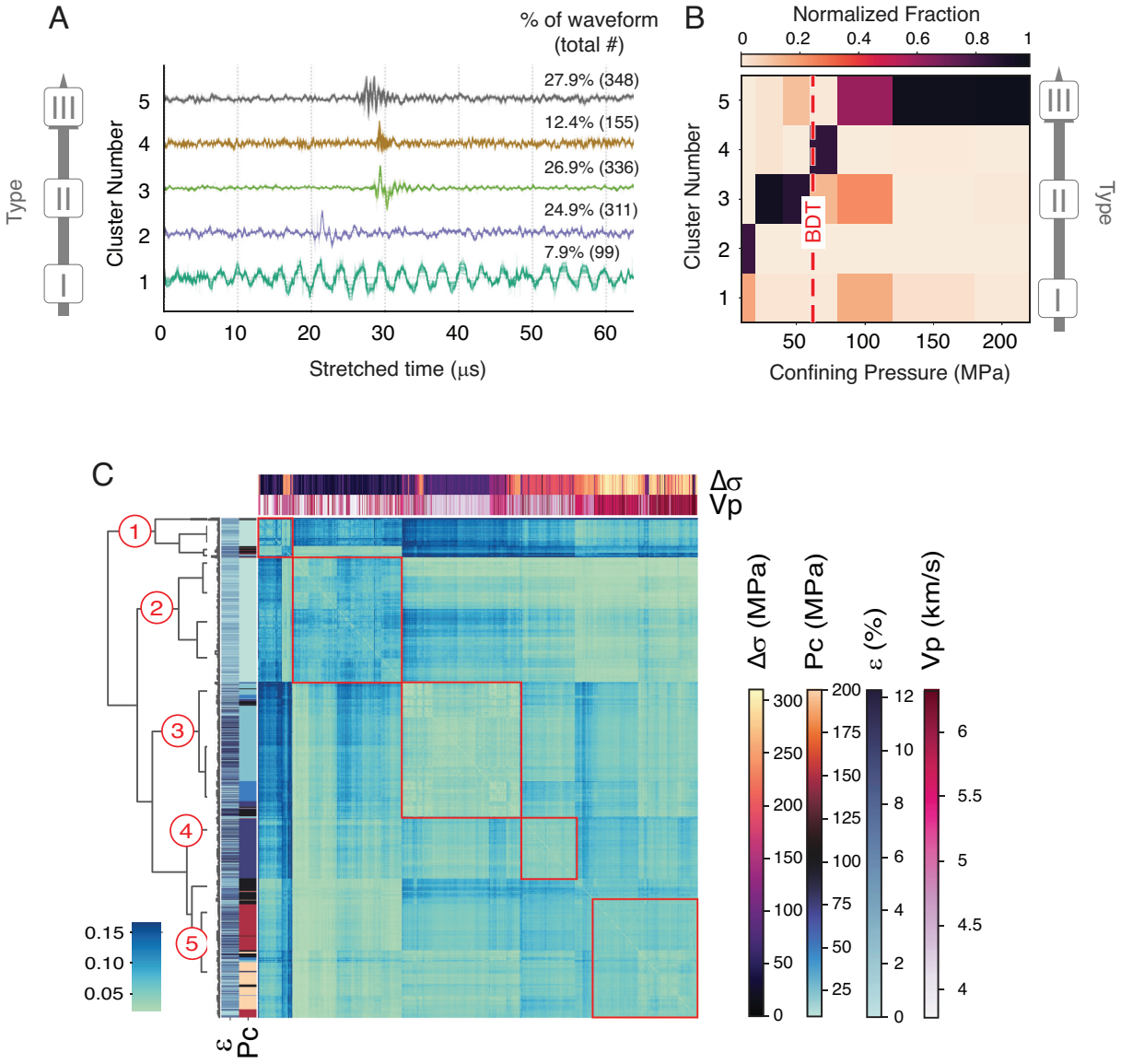

Fig. 2. Hierarchical clustering of acoustic data. (*A*) Representative waveforms for 5 global clusters further grouped into 3 types. (*B*) Occurrence of individual clusters at different confining pressures. The red dashed line indicates the location of the BDT in our experiments (*C*) Distance matrix and cluster dendrogram of all waveforms. The 1:1 diagonal is a correlation of a wave with itself. Several clusters of waveforms that occur under common conditions emerge as squares in the diagram. Red numbers in circles show characteristic clusters in the dendrogram; red squares highlight these clusters in the distance matrix. Each cluster can be further refined by higher-order differences between individual waveforms that are visualized as smaller squares within a larger cluster square and progressively finer branching in the dendrogram. Δσ–differential stress, Pc–confining pressure, ε–strain, Vp–longitudinal wave velocity.

and thus potentially similar class of microscale defects, we choose to group them together. Cluster 2 occurs exclusively at 10 MPa confining pressure, low stress, and low strain, whereas cluster 3 occurs predominantly at pressures ranging from 25 MPa to 100 MPa, intermediate stresses and intermediate strains, and cluster 4 occurs predominantly at 75 MPa confining pressure (Fig. 2 *B* and *C*). The number of events in cluster 3 decreases with increasing confining pressure. Both the duration as well as frequency of all type II events evolve with increasing pressure; at low pressures (10 and 25 MPa), the duration of type II events is ~2 to 5 μs, and the dominant frequency is ~2 MHz. At higher pressures (50, 75, 100, and 150 MPa), these events become shorter (from 1.2 to 0.4 μs), and their frequency increases to ~3, 7, 15 and 20 MHz respectively as presented in *SI Appendix*, Fig. S4.

Careful inspection of Type II signals shows additional, weak, high-frequency oscillations. These AE's, called Type III events (global Cluster 5), have additional peaks in the frequency domain and are usually superimposed on main type II signals. The type III events are particularly visible in cluster 4, less well developed in cluster 3 and absent in cluster 2 (Fig. 2 and *SI Appendix*, Fig. S5). The dominant frequency of these ultra-high-frequency acoustic emissions evolves with increasing pressure, from ~10 MHz to 20 MHz between P_c = 25 MPa and 50 MPa, eventually reaching 40 to 52 MHz at 200 MPa confining pressure (*SI Appendix*, Fig. S6).

The way that type II and type III signals combine follows a pattern that is closely correlated with the confining pressure. At 10 and 25 MPa, many type II events are "pure" or in combination with type I events, whereas at 50 MPa, a clear type III is linked to the tail of a dominant type II ripple. At yet higher pressures, approaching a more ductile regime, the higher-frequency type III signals are more interwoven within type II structure (*SI Appendix*, Figs. S4 and S5). Above 100 MPa confining pressure, type III signals occur independently of, simultaneously with, or ahead of type II wavelets, and hence, also form their own Cluster 5 (Fig. 2*A*). This cluster is typical for high confining pressures, high differential stresses, and high v_p (Fig. 1*C* and *SI Appendix*, Fig. S6).

Type III "wiggles" become common signal forms at 200 MPa confining pressure and appear more frequently during work hardening with avalanche-like patterns (Fig. 1*D* and *SI Appendix*, Fig. S6) Eventually, at higher mean stresses, these signals form semicontinuous emissions (*SI Appendix*, Fig. S6), a behavior typically observed during propagation of dislocation avalanches in metals (29–31). These AE bursts indicate successive motions with duration of each wavelet as short as ~200 ns. A considerable shift in frequency from ~45 MHz to ~52 MHz in type III signals during strain hardening is observed (*SI Appendix*, Fig. S7). A summary of the observed frequency ranges for each global cluster is displayed in *SI Appendix*, Fig. S8.

Discussion

The changes in waveform characteristics (characterized by the different AE Types) as well as the observed large frequency shifts as pressure increases and the rocks cross their BDT are probably linked to changes in the defect dynamics that cause the emissions. To estimate the importance of the path effect, we plot measured AE frequency against the nearest measured p-wave velocity in *SI Appendix*, Fig. S9 and observe no strong correlation suggesting that the source effect is indeed dominant in our data. To constrain this source effect, we use kinematic seismic source models to estimate the variations in front propagation velocity, v_f, and source size as an effective vibrating length, d_s from the measured frequency, ω. Here, we use the Savage model [(32); see *Materials and Methods* for a discussion of other models]:

$$\omega = \frac{(2v_p / d_s)(v_p^2 / v_f^2 + 0.5)^{0.5}}{v_p^2 / v_f^2 - 0.5},$$

to link the carrier frequency shifts of signals to the nature of the sources. To visualize the observed frequency shifts (Fig. 3), we plot the cumulative probability distribution functions of recorded AE frequencies at all confining pressures (Fig. 3*A*) and the mean stress ($(\sigma_1+\sigma_2+\sigma_3)/3$) vs. spectral power in the frequency domain (Fig. 3*C*). The shift in mean frequencies of sensor vibrations with increasing pressure and mean stress indicates that carrier frequencies of the events also generally increase (*SI Appendix*, Figs. S10 and S11). After estimating carrier frequencies of typical events from each deformation stage, we discuss the possible physics of the sources revealed by our analysis. In Fig. 3*B*, we plot the possible source dimension—propagation velocity isolines for frequencies measured at individual confining pressures together with physical bounds imposed by the sample size and elastic wave propagation velocities. Clearly, we find the characteristic source size decreases and/or propagation velocity increases with increasing confining pressure as the rocks reach a more ductile regime.

To further constrain the effective source size and mean velocity of defect propagation, we use information in recorded event amplitudes, *A*, at the sensor location considering attenuation effects ($\alpha(\omega, l_{ss})$), sensor parameters ($\{\Lambda\}$) and uncertainties in source locations (l_{ss})—see *Materials and Methods* for details and calibration of the model: $A_{\text{model}}(\omega, d_s, v_f, l_{ss}, \alpha, \{\Lambda\})$. In Fig. 3*D*, we show the flow of cluster amplitudes in $A(d_s, v_f)$ space in which we inferred values of d_s and v_f using measured amplitudes and frequencies of high signal-to-noise ratio (SNR) events (SNR > 3 to 4; see *Materials and Methods* and *SI Appendix*, Fig. S12). As confining pressure increases, cluster I signals (0.4 < ω < 7 MHz) broadly become less energetic, where low frequency, but energetic type I classes are more dominant at lower pressures. Therefore, we conclude that the effective nucleation size of type I sources decreases when the marble is deformed at higher pressures.

As confining pressure increases, type II signals (which includes clusters 2 to 4 in the frequency range 0.6 < ω < 30 MHz) typically show gains in velocity and reductions in effective source dimension. This source-size reduction begins to level off at higher pressures as marble transitions to a more ductile regime. With the increasing dominance of type III events at higher pressures, mean velocities and effective source dimensions both increase. In fact, moving towards type III events, the overall rate of energy radiation must increase as high-frequency events attenuate faster. Thus, type III events need to have a higher energy emission rate to be detectable. The lower envelope of observed events in the $A(d, v_f)$ space is likely a consequence of our detection sensitivity since it lies along a minimum amplitude contour in our model. However, we observe increasing event clustering, i.e., more localized clusters, in the d- v_f space with higher pressure (i.e., ductile regime). Conceptually, this observation suggests that the sources of dissipations are more uniform in the ductile regime compared to those in the low-pressure, brittle regime. Typically, we observe that Type III events occur in distinct, semicontinuous, emissions. Thus, we posit that the type III events might result from dislocation avalanches. The density of moving dislocations is proportional to $1/l^2$, where l is a length-scale characterizing the spatial distribution of dislocations as the distance between parallel slip lines (therefore effective $d_{source} \sim l$) (31, 33). Source sizes as small as 1 to 5 μm might

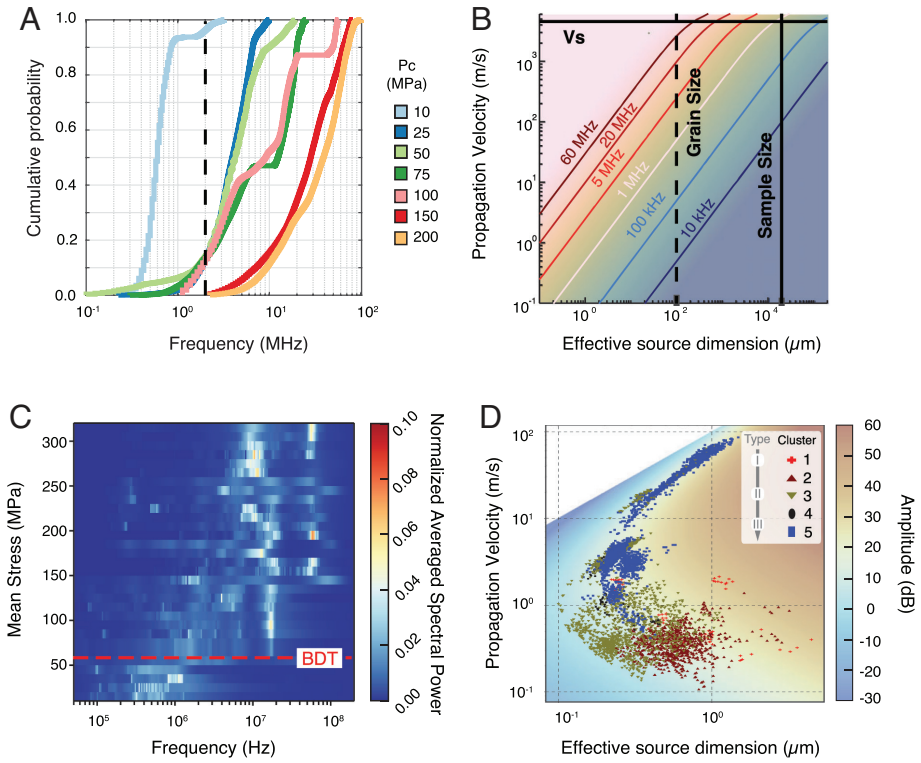

Fig. 3. Frequency Evolution of AEs and inferred defect size–propagation velocity relationships. (*A*) Cumulative distribution of frequencies indicates a progressive increase in mean frequency of acoustic waves with increasing pressure. The black dashed line shows the typical upper sensitivity limit of AE recordings in conventional rock mechanics experiments. (*B*) Observed frequency and inferred defect size–front propagation velocity relationship based on the Savage source model. Propagation velocity increases, and/or the mean source size decreases, with increasing confining pressure. *Vs* – transverse wave velocity. (*C*) Mean stress, $(\sigma_1+\sigma_2+\sigma_3)/3$ vs. spectral power at frequency. Note the progressive shift to higher frequencies with increasing mean stress. The red dashed line shows the location of the BDT in our experiments. (*D*) Flow of clusters in amplitude, A, propagation velocity, v_f and effective source dimension, d_{source} parameter space. The measured amplitudes and frequencies are used to infer effective source size and mean front velocity. The observed inflection point hints at the transition to a regime where the spread of clusters (in this space) becomes smaller, i.e., the characteristics of energy dissipation sources become more homogenous.

indicate dislocation densities of ~2×10^8 cm^{-2}—an order of magnitude comparable to the densities reported for deformed samples (18). Based on the above analyses, we hypothesize that the three main types of AEs correspond to three defect populations: cracks (type I), twins (type II), and dislocation avalanches (type III) as summarized in Fig. 4. All of these defects are commonly observed in postmortem observations of marbles deformed over this pressure range (3, 18, 19) and are known to produce AEs in various metals and ice (29–31). But, to date, this correlation of AE's and defect dynamics has not been reported for rocks. Further work is needed to firmly establish the connection between emitted waveforms and individual defect types in experiments where visual observation of defect activity is possible (*SI Appendix, Supplementary Text*) and then use this understanding to analyze finer scale waveform patterns (e.g., differences between local clusters).

In conclusion, our experimental results coupled with the AE clustering and frequency analysis strongly indicate that we can a) detect real-time signatures of the microscale defects during rock deformation and b) detect significant changes in AE signatures associated with the BDT of Carrara marble. We suggest that ultrasonic emissions carry information regarding the complexity of sources and that their interactions can be used to characterize crystal-plastic deformation as well as brittle processes. A critical, first-order observation from our experimental results is that accumulated AE count and AE energy follows a distinctly different pattern with strain (Fig. 1 and *SI Appendix*, Fig. S3) than the stress–strain curve. Considering the AEs as indicative of energy dissipation due to microscale defects, the AE datasets provide a real-time measure of dissipation instead of snapshots characteristic of the beginning and end of deformation, as is typically available from postmortem microstructural data. This opens up the exciting possibility of testing/calibrating scale-free visco-elasto-plastic rheological models using experimental energy dissipation measures and separating the microstructural contribution of elastic vs. various visco-plastic deformation processes using AE clusters. With further instrumental improvements, for example, increasing the SNR, increasing the frequency range, using a larger number of sensors for source location and moment tensor inversion, and improving harvesting of events in the noise level, etc., we envision that our approach can be employed to improve our understanding of defect dynamics and to aid the development of a new generation of microstructural process-guided rheological models for rocks. With development of high-temperature piezo-sensors, we expect that dynamic signatures of defects can be detected also in silicate rocks, which are more abundant on Earth than carbonates.

Materials and Methods

We deformed cylindrical samples (10 mm in diameter and 20 mm in length) of dry Carrara marble in a Paterson gas-medium, deformation apparatus under conventional triaxial loading (34) (*SI Appendix*, Fig. S13 and Table S1). We applied confining pressures ranging from 10 MPa to 200 MPa, which is sufficient to cross the BDT at room temperature (3, 7) (*SI Appendix*, Figs. S1 and S14). In all our experiments, we used two custom-made, miniature piezo-sensors on top and bottom of the sample, covering a broad range of frequencies (from 70 kHz to 65 MHz). Sensor response is shown in *SI Appendix*, Figs. S15–S17. We used these sensors to measure the evolution of longitudinal wave velocities (v_p) in active mode (*SI Appendix*, Figs. S18 and S19) and to record acoustic emissions in

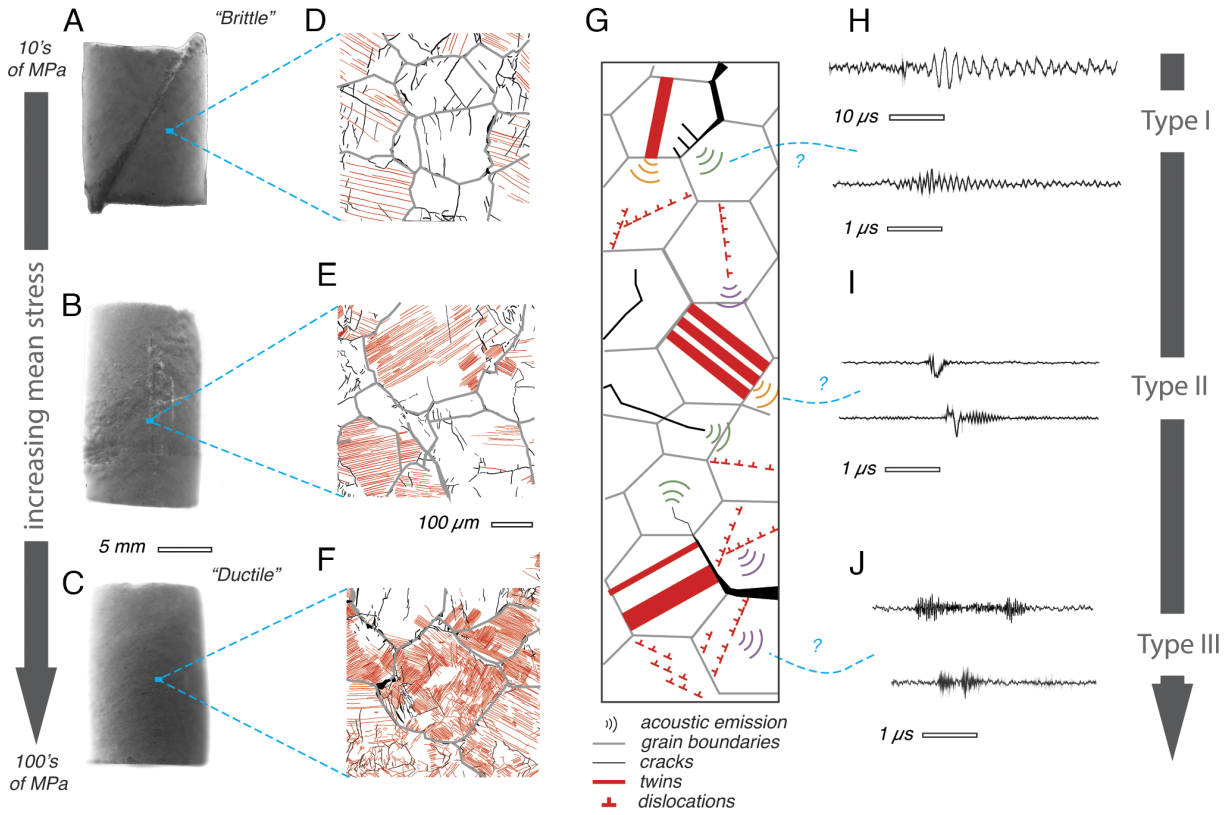

Fig. 4. Summary of observations. (*A–C*) The final appearance of the sample after deformation at a fixed pressure. At higher pressures, the deformation is dispersed through the sample and no faults formed. (*D–F*). Characteristic microstructures. Note how defect density increases and crystal plastic defects become more abundant with increasing mean stress. Gray–grain boundaries, red–crystal plastic defects (slip lines and twins), black–brittle defects (microcracks and pores). (*G*) Schematic of microstructural processes occurring during deformation and their postulated ultrasound signatures (*H–J*).

passive mode during the experiment. We source located some of the AEs along the sample height using measured sound velocities and signal arrival times (*SI Appendix*, Fig. S20).

Microstructure Analysis. To document the main defect types operating in the brittle as well as ductile regime, we performed two experiments using split cylinders deposited with a regular microscale grid with a spacing of 10 μm using the "microscale strain measuring technique" (MSSM) (35). MSSM allows us to analyze the same areas before and after deformation and document changes that occurred during the experiment. To quantify the density and orientation of individual defects, we manually trace the features on optical high-magnification (700×) images. We analyze the shape preferred orientation (SPO) of both cracks and crystal-plastic deformation features (twins and slip lines) using the "paror" and "surfor" methods that rely on the projection of the digitized features to extract both the preferred orientation(s) as well as the strength of the SPO (36). An isotropic shape would give a constant projection function of b/a = 1 and round characteristic shape, a line will have sharp minima of b/a = 0 at a given angle, θ, which corresponds to the SPO. Microstructural observations document abundant microcracks that are dominantly oriented parallel to the loading direction suggesting mode I cracking irrespective whether a macroscopic fault developed. As shown in *SI Appendix*, Fig. S2, the SPO is stronger and the area affected by cracks is larger at lower pressures than at higher pressures (aspect ratio, b/a, of the fabric is 0.64 vs. 0.72 and the crack density is 89.3 ± 7.7 mm^2/mm^3 vs. 35.2 ± 2.6 mm^2/mm^3 at Pc = 25 MPa and 75 MPa respectively). Crystal-plastic defects form a strong SPO inclined oblique to the loading axis close to the orientation of maximum resolved shear stress and exhibit a monoclinic characteristic shape. The density of these defects significantly increases from 17.1 ± 5.8 #/mm to 98.9 ± 22.4 #/mm at Pc = 25 and 75 MPa, respectively (*SI Appendix*, Fig. S2 *B* and *E*).

Attenuation Considerations. Marble's attenuation coefficient, α, quantifies the energy loss with wave propagation distance. As a first-order approximation, attenuation is linearly related to frequency as $\alpha \sim \beta\omega$. We define $dB = 20 \times \log(V/V_{ref})$ where V is the measured voltage amplitude, V_{ref} is a reference voltage, and the coefficient β is ~1.125. We hence assume that marble does have an approximately linear frequency spectrum with low attenuation as observed in previous work (37, 38). As a first approximation, we assume $v_p = 6$ km/s and consider the variation of velocity to be trivial (for high confining pressure >100 MPa tests this variation is less than 10%).

We now estimate how detectability of signals is affected due to the attenuation of high-frequency waves: $\alpha = \frac{dB}{cm} = \frac{dB}{v_p t} = \beta\omega$; then $\frac{dB}{t} = v_p\beta\omega = 0.81\omega$ (attenuation per micro-second). Assume that the maximum radiation amplitude field in vicinity of the source is A_{max}^{source} (in mV) and that the distance of the source to the sensor is l_{ss}; the amplitude of the first arrival in the sensor location then reads as follows: $A_{sensor}(t = t_{p-arrival})\ [in\ dB] = 20\log\left(\frac{A_{max}^{source}}{A_{ref}}\right) - 0.81\omega \times l_{ss} \times v_p^{-1}$; assuming $A_{ref} \equiv 1$ we get $A_{sensor}(t = t_{p-arrival})\ [in\ dB] = 20\log\left(A_{max}^{source}\right) - 0.81\omega \times l_{ss}(cm) \Rightarrow A_{sensor-mv} = 10^{\log(A_{max}^{source}) - 0.066\times\omega\times l_{ss}(cm)}$ (the later equation is in linear scale and not in dB units).

Now let us assume a background noise level (nl) with amplitude of $A_{nl}(\omega)$. To be able to record the first peak above the noise level (without considering amplification of signals), one should satisfy a minimum condition irrespective of the intensity of the source: $A_{sensor}(t = t_{p-arrival}) > A_{nl}(\omega)$, which leads to $A_{sensor}(t = t_{p-arrival}) > A_{nl}(\omega) \Rightarrow 10^{\log(A_{max}^{source}) - 0.066\times\omega\times l_{ss}(cm)} > A_{nl}(\omega) \Rightarrow A_{max}^{source} > A_{nl}(\omega) \times 10^{0.066\times\omega\times l_{ss}(cm)}$.

This inequality relation gives a minimum condition of signal detectability without considering amplification of signals. Further, we assume the noise level is ~100 μV (at 1 MHz) and reaches to ~220 μV (at 60 MHz). Approaching longer distance and higher frequency, the minimum power of radiation in the source point should increase to satisfy crossing the noise level. Applying 50-dB amplification and above to the receiver sensor, the signals up to ~50 MHz and distances as far as 10 mm will be detectable. Considering the variation of electrical noise level and potential nonlinearity of α dependent to higher-orders of frequency in poly-crystalline materials due to scattering loss (37, 38), we expect

that probability of recording emissions in full length of the sample decreases rapidly with increasing emissions frequency. In conclusion, we expect that attenuation will make it more challenging to detect (ultra) high-frequency AEs. More accurately, according to a theoretical model for longitudinal wave scattering in poly-crystalline materials, three scattering regimes are recognized based on wavelength of signals (λ_l): 1) $\lambda_l \gg 2\pi\overline{D}$ as Rayleigh scattering regime, 2) $\lambda_l \sim 2\pi\overline{D}$ as stochastic scattering regime, and 3) $\lambda_l \ll 2\pi\overline{D}$ diffused scattering regime in which $\overline{D}$ is the average size of grains. Considering $\overline{D} \approx 100\,\mu m$, $\lambda_l = v_p\omega^{-1}$ and $v_p = 6$ km/s, the Rayleigh scattering regime falls in $\omega \ll 60$ MHz. As an approximation, when the wavelength is larger than three times the grain size ($\lambda \gg 300\,\mu m \rightarrow \omega \ll 20$ MHz), the attenuation as a function of frequency evolves in the form of ω^2 (38). For higher frequencies, the attenuation due to scattering loss becomes independent of frequencies. We have ignored such nonlinearity in the above calculations and approximated a linear attenuation rate.

Data Processing: DTW and Hierarchical Clustering. We use the DTW (39–41) distance measure to compare the similarity of different waveforms across the experiments. The DTW algorithm finds the temporal alignment between two waveforms (by allowing nonlinear stretching) that minimizes Euclidean distance between them when aligned, as illustrated in Supplementary *SI Appendix*, Fig. S21. The waveforms are "warped" nonlinearly in the time dimension to determine a measure of their similarity independent of certain nonlinear variations (stretching, shifting) in the time dimension. The final DTW distance measure is the Euclidean distance between the target and the warped waveforms.

We use DTW as the distance measure for our analysis since its properties allow us to address two key challenges in our dataset: a) different length of the AE waveforms for different datasets due to changing event durations, and b) strongly changing frequency content of the AE waveforms as a function of pressure. These characteristics make the DTW distance different from the more standard cross-correlation–based methods that are commonly used in seismic data analysis. Thus, using DTW distance can allow us to statistically compare the waveform shapes in the experimental datasets from 10 MPa to 200 MPa confining pressure by calculating nonlinear stretching to compare waveforms with very different dominant frequencies. This enables us, as shown in Figs. 1 and 2, to find characteristic AE waveform shapes on the local (i.e., within each individual experiment) as well as global (i.e., on all emissions form all experiments) level. For our final analysis, we compute the DTW distance for each waveform pair and then normalize by the length of the longest waveform (in the pair) to get a normalized DTW distance that is insensitive to the length of the original waveforms (to prevent trivial grouping of data from individual experiments together). We have tested the accuracy of this approach using synthetic waveform datasets with waveforms of different lengths. Recent studies have shown that in many cases, DTW, which has a higher computational cost, is a superior distance metric for time series clustering when compared to cross-correlation or direct distance measures between unstretched waveforms (42).

With the full-normalized DTW distance matrix (shown in Fig. 2), we use the hierarchical clustering algorithm to group the waveforms into representative clusters in an unsupervised manner (43). We use the agglomerative hierarchical clustering (AHC) algorithm since it organizes the waveform datasets with a bottom–up approach: It first combines the two closest waveforms into a cluster and progressively repeats this grouping until the whole dataset is clustered into increasingly larger groups as shown by the different levels of the dendrogram in Fig. 2. Thus, the AHC allows us to naturally see the waveforms relationship across different levels of similarity. The merging of waveforms into clusters in the algorithm is determined by the linkage criterion. For the analysis in our study, we use the Ward linkage method (44).

Ward's method seeks to choose members of clusters in a way that minimize the increase in the sum of squared differences within each cluster. This variance-minimizing approach is conceptually similar to the k-means clustering method. Although there are a number of other potential linkage function choices (e.g., single, complete, median), Ward linkage is observed to typically produce the most meaningful and balanced clusters for numerical data (45). We systematically compared the results of the clustering analysis using the other linkage choices and find that AHC with Ward linkage provides the most meaningful waveform clusters. The other key parameter for the final clustering is choosing the number of clusters. Classically, the AHC analysis uses a cut of the dendrogram at a chosen DTW distance to determine the cluster assignment. However, this approach has the challenge that it weights the clustering to separate out the more outlier events first in the first few clusters, and a large number of clusters (typically > 6) are needed to discern the more subtle waveform differences we are interested in. Thus, after careful analysis of clustering results with number of clusters ranging from 3 to 10, we chose a nonsingular distance cut of the dendrogram to determine the cluster assignment. Although we acknowledge that this approach is subjective, we find that this improves the clustering interpretability significantly. Additionally, this conceptual approach has been explored in some of the newer, density-based clustering algorithms (46). This is an area of active research for improving the accuracy of hierarchal clustering algorithms and making them less sensitive to a few noisy events.

Note that we do not use the spectrogram or other frequency-based methods for waveform classification since the experiments at different pressures have very different frequencies. The spectrograms are shown in *SI Appendix*, Fig. S22 and illustrate the spatiotemporal differences in the frequency content of each representative waveform.

Estimation of Source Size and Propagation Velocity From Frequency of Emissions. To relate frequency of emitted waves to various source models, one must consider the full sensor response where the amplitude-time of recorded waveforms are mixed responses of sensor assembly, rock itself, and source. We have therefore calibrated the low-frequency sensor employed in our tests using a laser Doppler vibrometer. Calibration results indicate that the rise portion of the signal (defined as the p-wave arrival to maximum amplitude of the first motion) scales roughly with particle velocity dominated by out-of-plane component [(47) and *SI Appendix*, Fig. S17]. We assume the same calibration holds for high-frequency sensors. To elaborate on the rise time of sensors, we used ball drop tests with different release heights and confirm that the rise time correlates with the colliding velocity (and then contact time) of the balls. Slower collision velocity results in longer rise time, whereas faster collision at the interface yields shorter rise time. In our analysis, we assumed the signal's corner frequency is the same as corner frequency employed in the tested theoretical model. We note that transition in dominant frequency of signals is not sensor dependent; keeping the same sensor set-up (both top and bottom sensors) and changing the confining pressures results in clear shifts to higher-frequency emissions.

The Savage model assumes a rectangular source with a width of W which propagates ($W \times l$: size of source). The front travels half-width in t–time with velocity, v_f; t is assumed to be rise time in longitudinal signal. The corner (angular) frequency in a given direction from source is given by: $\omega = \frac{(2v_p/d_s)(v_p^2/v_f^2+\cos^2\theta)^{0.5}}{v_p^2/v_f^2-\cos^2\theta}$, in which v_p is the P-wave velocity and v_f is the front velocity; d_s is the size of the source. In Fig. 3*B*, we plotted the frequency-source size at $\theta = \pi/4$ (source propagates at an angle to sensor) based on Marble parameters up to frequencies of 60 MHz.

Several source models exist; another established model [Sato-Hirasawa (48)] uses a circular source and gives the following relation: $\omega = \frac{f(v_f/c)c}{l}$, where function f is a coefficient dependent on front velocity. This model estimates slightly higher-frequency emissions for a given source size-front velocity pair than the Savage model. Furthermore, Madariaga's numerical model (49) estimates frequency of emissions from a circular propagating source (with radius of l) as $\omega = \frac{kv_f}{l}$ where k is a constant. Madariaga's solution gives intermediate values for $\omega(v_f, l)$ with $k \sim 2$ for the front velocity of $0.9v_p$. In summary, while different source models yield slightly different source size–front propagation velocity isolines for a given frequency, all share the general characteristic that higher frequencies imply faster propagation and/or smaller source size.

Estimate of Source Parameters from Event Amplitude. Now, we consider amplitude of events recorded in the sensor location assuming an ideal 1D model of marble, while we use both attenuation as well as source kinematics information. The amplitude (in Volt) at distance, l_{ss}, from the source of the size d_{source} is given roughly by relationship (38): $A \approx \chi\Lambda d_{source} v_f t_{sensor}$, where Λ is related to the piezoelectric voltage constant (Volt/m; $\Lambda^{-1} \sim 127$ pm/V), t is inverse of resonance frequency of the piezo-ceramic (~0.02 μs for high-frequency sensor), and X is the coefficient related to ratios of acoustic impedances of the sensor and rock (we consider imperfect mismatch $X \approx 0.5$). Combining this relationship with $\omega = \frac{kv_f}{l}$ and the estimated attenuation correction, we approximate the recorded amplitude

as $A_{dB} \approx 20\log\frac{\Lambda t\omega d^2_{source}}{2} - \beta l_{ss}\omega$, where we implemented the effect of attenuation as $\beta l_{ss}\omega$. An extra amplification term must be added to the above relationship for comparison with the recorded events from marble deformation. Then, if the distance from source to sensor (l_{ss}) and recorded amplitude is known for a given sensor, observed frequency changes will yield source size and therefore, average velocity of fronts. Two further steps are considered to faithfully use this model on our marble data set: 1) to validate the estimates from this model, we used recorded signals and fast-camera videos (recorded at 6,400 frames per second) on evolving features observed during deformation of a calcite single crystal at room pressure (*SI Appendix*, Figs. S23 and S24). In *SI Appendix*, Fig. S24, we show the validation of the amplitude estimate measuring mean velocity of two fronts and corresponding emitted waves: a) a slow front with average velocity of ~0.3 m/s with emitted wave of frequency ~200 kHz (Movie S1) and b) a faster defect front where each branch evolves as fast as $v_f = 10$ to 50 m/s with a frequency of ~1.2 MHz (Movie S2). 2) Errors due to uncertainties in source–sensor distance as well as sensor response and coupling effects. We use realizations of 20 randomly located events and plot average of $A_{\text{model}}(\omega, d_s, v_f, l_{ss}, \alpha, \{\Lambda\})$. Note, that the parameter, A_{model}, ideally reflects the particle velocity in the sensor location. However, due to nonuniform response of any piezo-sensor, exact transformation of measured amplitudes to true amplitudes requires more sensor response evaluation at frequencies as high as 60 MHz. However, we still expect that the overall $A(d,v_f)$ pattern to remain as more accurate sensor calibrations are obtained, but the effective source dimension could be larger (within a factor of 5 to 10). We use a SNR threshold of 4 (and SNR threshold of 3 for 100 MPa events to allow few more events) for our primary analysis and choose all the spectral power peaks within 3 to 4 dB of the peak value. Our primary results are not sensitive to these specific parameter choices and have been chosen to maximize unbiased inclusion of high-quality events in our analysis. To estimate the peak spectral amplitude and frequency, we use the empirical mode decomposition and Hilbert–Huang spectral analysis method (50).

Data, Materials, and Software Availability. All study data are contained in the article and/or supporting information. These data can also be found in digital form in ref. (51).

ACKNOWLEDGMENTS. H.O., M.P., and T.M. would like to thank Ben Holtzman for stimulating discussions on "machine listening" during numerous group meetings. Discussion of an early version of the paper with T. Grove, O. Jagoutz, B. Hager, and G. Dresen helped us to improve the paper. We also thank Alejandra Quintanilla Terminel for providing the gridded cylinders used for microstructural analysis and Camilla Cattania for discussion of source models. T.M. acknowledges support by the Crosby Fellowship at MIT, M.P. acknowledges funding by MIT's J.H. and E.V. Wade Fund. "CORD" Laboratory technician support was provided by NSF–2054414 to M.P. and B.E.

1. D. L. Kohlstedt, B. Evans, S. J. Mackwell, Strength of the lithosphere: Constraints imposed by laboratory experiments. *J. Geophys. Res.* **100**, 517–587 (1995).
2. R. Bürgmann, G. Dresen, Rheology of the lower crust and upper mantle: Evidence from rock mechanics, geodesy, and field observations. *Annu. Rev. Earth Planet. Sci.* **36**, 531–567 (2008).
3. B. Evans, J. T. Fredrich, T. Wong, "The brittle-ductile transition in rocks: Recent experimental and theoretical progress" in *The Brittle-Ductile Transition in Rocks*, A. G. Duba, W. B. Durham, J. W. Handin, H. F. Wang, Eds. (*Geophysical Monograph Series*, American Geophysical Union, Washington, DC, 1990), pp. 1–20.
4. M. Pec, H. Stünitz, R. Heilbronner, M. Drury, Semi-brittle flow of granitoid fault rocks in experiments. *J. Geophys. Res. Solid Earth* **121**, 1677–1705 (2016).
5. E. H. Rutter, On the nomenclature of mode of failure transitions in rocks. *Tectonophysics* **122**, 381–387 (1986).
6. E. Aharonov, C. H. Scholz, The Brittle-Ductile transition predicted by a physics-based friction law. *J. Geophys. Res. Solid Earth* **124**, 2721–2737 (2019).
7. G. G. Meyer, N. Brantut, T. M. Mitchell, P. G. Meredith, Fault reactivation and strain partitioning across the brittle-ductile transition. *Geology* **47**, 1127–1130 (2019).
8. F. Giuntoli, G. Viola, Cyclic brittle-ductile oscillations recorded in exhumed high-pressure continental units: A record of deep episodic tremor and slow slip events in the northern Apennines. *Geochem. Geophys. Geosyst.* **22**, e2021GC009805 (2021).
9. M. E. Oliveira *et al.*, Impact of crustal rheology and inherited mechanical weaknesses on early continental rifting and initial evolution of double graben structural configurations: Insights from 2D numerical models. *Tectonophysics* **831**, 229281 (2022).
10. A. R. Cruden, R. F. Weinberg, "Mechanisms of magma transport and storage in the lower and middle crust–magma segregation, ascent and emplacement" in *Volcanic and Igneous Plumbing Systems*, S. Burchardt, Ed. (Elsevier, 2018), pp. 13–53.
11. D. L. Kohlstedt, L. N. Hansen, Treatise on geophysics. https://doi.org/10.1016/B978-0-444-53802-4.00042-7 (25 August 2015).
12. M. S. Paterson, T. Wong, *Experimental Rock Deformation-The Brittle Field* (Springer, Berlin, Heidelberg, ed. 2, 2005).
13. F. Renard, N. Kandula, J. McBeck, B. Cordonnier, Creep burst coincident with faulting in marble observed in 4-D synchrotron X-ray imaging triaxial compression experiments. *J. Geophys. Res. Solid Earth* **125**, e2020JB020354 (2020).
14. S. J. Covey-Crump, P. F. Schofield, E. C. Oliver, Using neutron diffraction to examine the onset of mechanical twinning in calcite rocks. *J. Struct. Geol.* **100**, 77–97 (2017).
15. D. Amitrano, Brittle-ductile transition and associated seismicity: Experimental and numerical studies and relationship with the b value. *J. Geophys. Res. Solid Earth* **108**, 0148–0227 (2003).
16. M. Knezevic, I. J. Beyerlein, D. W. Brown, T. A. Sisneros, C. N. Tomé, A polycrystal plasticity model for predicting mechanical response and texture evolution during strain-path changes: Application to beryllium. *Int. J. Plast* **49**, 185–198 (2013).
17. B. Richter, H. Stünitz, R. Heilbronner, The brittle-to-viscous transition in polycrystalline quartz: An experimental study. *J. Struct. Geol.* **114**, 1–21 (2018).
18. J. T. Fredrich, B. Evans, T. Wong, Micromechanics of the brittle to plastic transition in Carrara marble. *J. Geophys. Res. Solid Earth* **94**, 4129–4145 (1989).
19. E. Rybacki, L. Niu, B. Evans, Semi-brittle deformation of Carrara marble: Hardening and twinning induced plasticity. *J. Geophys. Res. Solid Earth* **126**, e2021JB022573 (2021).
20. N. Kandula *et al.*, Dynamics of microscale precursors during brittle compressive failure in Carrara marble. *J. Geophys. Res. Solid Earth* **124**, 6121–6139 (2019).
21. C. Parlangeau, A. Dimanov, O. Lacombe, S. Hallais, J.-M. Daniel, Uniaxial compression of calcite single crystals at room temperature: Insights into twinning activation and development. *Solid Earth* **10**, 307–316 (2019).
22. J. H. P. De Bresser, C. J. Spiers, Strength characteristics of the r, f, and c slip systems in calcite. *Tectonophysics* **272**, 1–23 (1997).
23. M. F. Ashby, S. D. Hallam, The failure of brittle solids containing small cracks under compressive stress states. *Acta Metal.* **34**, 497–510 (1986).
24. Y. Bernabé, M. Pec, Brittle creep and failure: A reformulation of the wing crack model. *J. Geophys. Res. Solid Earth* **127**, e2022JB024610 (2022).
25. J.-P. Poirier, *Creep of Crystals: High-Temperature Deformation Processes in Metals, Ceramics and Minerals* (Cambridge University Press, 1985).
26. A. Schubnel *et al.*, Transient creep, aseismic damage and slow failure in Carrara marble deformed across the brittle-ductile transition. *Geophys. Res. Lett.* **33**, L17301 (2006).
27. D. Lockner, The role of acoustic emission in the study of rock fracture in. *Int. J. Rock Mech. Mining Sci. Geomech. Abst.* **30**, 883–899 (1993).
28. X. Lei, K. Kusunose, T. Satoh, O. Nishizawa, The hierarchical rupture process of a fault: An experimental study. *Phys. Earth Planet. Inter.* **137**, 213–228 (2003).
29. A. Vinogradov, D. Orlov, A. Danyuk, Y. Estrin, Effect of grain size on the mechanisms of plastic deformation in wrought Mg–Zn–Zr alloy revealed by acoustic emission measurements. *Acta Mater.* **61**, 2044–2056 (2013).
30. Y. Chen *et al.*, Multiple avalanche processes in acoustic emission spectroscopy: Multibranching of the energy–Amplitude scaling. *Phys. Stat. Solidi* **259**, 2100465 (2022).
31. J. Weiss, J.-R. Grasso, Acoustic emission in single crystals of ice. *J. Phys. Chem. B* **101**, 6113–6117 (1997).
32. J. C. Savage, Relation of corner frequency to fault dimensions. *J. Geophys. Res.* **77**, 3788–3795 (1972).
33. V. Boyko, R. Garber, A. Kossevich, *Reversible Crystal Plasticity* (Springer Science & Business Media, 1997).
34. M. S. Paterson, Rock deformation experimentation. The Brittle-Ductile transition in rocks. *Geophys. Monogr. Ser.* **56**, 187–194 (1990).
35. A. Quintanilla-Terminel, B. Evans, Heterogeneity of inelastic strain during creep of Carrara marble: Microscale strain measurement technique. *J. Geophys. Res. Solid Earth* **121**, 5736–5760 (2016).
36. R. Heilbronner, S. Barrett, *Image Analysis in Earth Sciences: Microstructures and Textures of Earth Materials* (Springer Science & Business Media, 2014).
37. S. Peacock, C. McCann, J. Sothcott, T. R. Astin, Experimental measurements of seismic attenuation in microfractured sedimentary rock. *Geophysics* **59**, 1342–1351 (1994).
38. K. Ono, A comprehensive report on ultrasonic attenuation of engineering materials, including metals, ceramics, polymers, fiber-reinforced composites, wood, and rocks. *Appl. Sci.* **10**, 2230 (2020).
39. H. Sakoe, S. Chiba, Dynamic programming algorithm optimization for spoken word recognition. *IEEE Trans. Acoust. Speech Signal Process.* **26**, 43–49 (1978).
40. M. Yadav, M. A. Alam, Dynamic time warping (dtw) algorithm in speech: A review. *Int. J. Res. Electron. Comp. Eng.* **6**, 524–528 (2018).
41. P. Senin, Dynamic time warping algorithm review. *Information and Computer Science Department University of Hawaii at Manoa Honolulu, USA* **855**, 40 (2008).
42. U. Kumar, C. P. Legendre, L. Zhao, B. F. Chao, Dynamic time warping as an alternative to windowed cross correlation in seismological applications. *Seismol. Soc. Am.* **93**, 1909–1921 (2022).
43. F. Murtagh, P. Contreras, Algorithms for hierarchical clustering: An overview. *Wiley Interdiscip. Rev. Data Min. Knowl. Discov.* **2**, 86–97 (2012).
44. J. H. Ward Jr., Hierarchical grouping to optimize an objective function. *J. Am. Stat. Assoc.* **58**, 236–244 (1963).
45. S. Sharma, N. Batra, "Comparative study of single linkage, complete linkage in and ward method of agglomerative clustering" in *2019 International Conference on Machine Learning, Big Data, Cloud and Parallel Computing (COMITCon), Faridabad, India* (IEEE, 2019), pp. 568–573.
46. R. J. G. B. Campello, D. Moulavi, J. Sander, "Density-based clustering based on hierarchical density estimates" in *Pacific-Asia Conference on Knowledge Discovery and Data Mining*, J. Pei, V. S. Tseng, L. Cao, H. Motoda, G. Xu, Eds. (Springer, Berlin, Heidelberg, 2013), pp. 160–172.
47. H. O. Ghaffari, U. Mok, M. Pec, On calibration of piezoelectric sensors with laser doppler vibrometer. *J. Acoust. Soc. Am.* **150**, 2503–2513 (2021).
48. T. Sato, T. Hirasawa, Body wave spectra from propagating shear cracks. *J. Phys. Earth* **21**, 415–431 (1973).
49. R. Madariaga, Dynamics of an expanding circular fault. *Bull. Seismol. Soc. Am.* **66**, 639–666 (1976).
50. A. J. Quinn, V. Lopes-dos-Santos, D. Dupret, A. C. Nobre, M. W. Woolrich, EMD: Empirical mode decomposition and Hilbert-Huang spectral analyses in Python. *J. Open Source Softw.* **6**, 2977 (2021).
51. H. O'Ghaffari *et al.*, Microscopic defect dynamics during a brittle-to-ductile transition [Data set]. Zenodo. https://doi.org/10.5281/zenodo.8384416. Deposited 27 September 2023.